Tomographic reconstruction of the small-angle x-ray scattering tensor with filtered back projection

Kim, J.; Pelt, D.M.; Kagias, M.; Stampanoni, M.; Batenburg, K.J.; Marone, F.

Tomographic Reconstruction of the Small-Angle X-Ray Scattering Tensor with Filtered Back Projection

Jisoo Kim,[1,2] Daniël M. Pelt,[3] Matias Kagias,[4] Marco Stampanoni,[1,2] K. Joost Batenburg,[3,5] and Federica Marone[2,*]

[1] *Institute for Biomedical Engineering, ETH Zürich, Zürich 8092, Switzerland*
[2] *Swiss Light Source, Paul Scherrer Institut, Villigen 5232, Switzerland*
[3] *Leiden Institute of Advanced Computer Science, Leiden University, Leiden, Netherlands*
[4] *Division of Engineering and Applied Science, California Institute of Technology, Pasadena, California 91125, USA*
[5] *Computational Imaging Group, Centrum Wiskunde & Informatica, Amsterdam 1098 XG, Netherlands*

(Received 26 January 2022; revised 3 May 2022; accepted 2 June 2022; published 19 July 2022)

Small-angle x-ray scattering tensor tomography provides three-dimensional information on the unresolved material anisotropic microarchitecture, which can be hundreds of times smaller than an image pixel. We develop a direct filtered back-projection method based on algebraic filters that enables rapid tensor-tomographic reconstructions and is a few orders of magnitude faster compared to established techniques, given the same computational resources. We demonstrate the accuracy of the method on experimental data for a fiber-reinforced material sample. The achieved acceleration may pave the way toward the investigation of multiple large samples as well as rapid control and feedback during *in situ* tensor-tomographic experiments, opening perspectives for the understanding of the fundamental link between functional material properties and microarchitecture.

DOI: 10.1103/PhysRevApplied.18.014043

I. INTRODUCTION

The macroscopic properties of both synthetic and natural materials are dictated by their micro- and nanosized structures. The mechanical behavior of biological samples [1,2] and bioinspired synthetic [3] and processed wooden materials [4], as well as the functional network of the brain [5], are directly linked to the local orientation of their microstructures. Also, the local orientation and degree of alignment of microfibers dictate the mechanical, thermal, and electrical properties of fiber-reinforced composite materials [6–8]. Information on the micro- and nanoscopic architecture in an extended field of view (FOV) is therefore valuable for a deeper understanding of existing materials, for the development of new tailored materials, and for product quality control in industry. Typically, the FOV is limited to just a few thousand times the image pixel size, while this should be at least twice as small as the structure size of interest [9]. Small-angle x-ray scattering (SAXS) contrast effectively decouples the structure size of interest and the accessible FOV: micro- and nanostructures can be investigated over a significantly larger FOV [10–12] and the length scale of interest can be hundreds of times smaller than an image pixel. Following early work [13], SAXS tensor tomography has emerged as a powerful imaging technique that reveals anisotropic micro- and nanostructures in large samples in three-dimensional (3D) [14–19]. The potential of scattering-tensor tomography has been shown for biomedical [20–22] as well as for industrial applications [23,24].

The scattering intensity depends on the relative orientation between the x-ray path and the measured anisotropic structure. In addition, the probed scattering intensity depends on the sensitivity direction of the detection mechanism. Due to this rotational dependence of the scattering signal, an analytical solution for tensor-tomographic reconstruction has not been established so far. For limited cases, experiments can be carefully designed so that the scattering intensity is measured with an approximated rotational invariance [17,25] and a tensor-tomographic reconstruction can be performed through multiple filtered back projections (FBPs) [26]. However, this requires measurements of the sample subsequently rotating around numerous rotation axes uniformly distributed on a unit sphere, leading to long acquisitions. Volume registration of the reconstructed volumes obtained from different rotation axes is also necessary, which increases the computation time and the complexity of the reconstruction pipeline. All other existing reconstruction algorithms for tensor tomography are based on algebraic methods [14–19,27–30] that

*federica.marone@psi.ch

are computationally heavy due to the need for repetitive forward and back projection. Efficient parallelization for different iteration steps is not straightforward due to the sequential nature of these methods. Thus, tensor-tomographic reconstruction algorithms typically require hours to days for computation and up to weeks for data with tens to hundreds of time points.

Recently developed circular diffractive optics with omnidirectional sensitivity have enabled single-shot ultra-small-angle x-ray scattering (USAXS) imaging [31–33]. Even though rapid-acquisition strategies based on these advanced optics have been developed aiming at *in situ* measurements [34,35], the long reconstruction time has hindered rapid (within seconds) control and feedback of tensor-tomography experiments. The lack of rapid access to even preliminary reconstructions often leads to suboptimal results, which are difficult to repeat at a later time for experiments at synchrotron facilities due to their competitive accessibility, limiting the potential of the technique.

To overcome these limitations, we propose a direct FBP reconstruction method for tensor tomography that is as fast as an analytical reconstruction and enables fast feedback and control of tensor-tomography experiments. The method utilizes a precomputed filter that accurately approximates any linear-shift-invariant (LSI) iterative reconstruction algorithm [36,37] and is compatible with an arbitrarily complex acquisition trajectory, without requiring stringent dense and uniform sampling. This algebraic filter depends only on the acquisition geometry, is independent from the samples, and therefore can be precomputed and reused. The orders-of-magnitude reduction in computation time, coupled with the recent experimental advancements [31–35], hopefully has the capacity to unleash the full potential of tensor tomography, enabling rapid access to microarchitecture in multiple, large, and evolving samples.

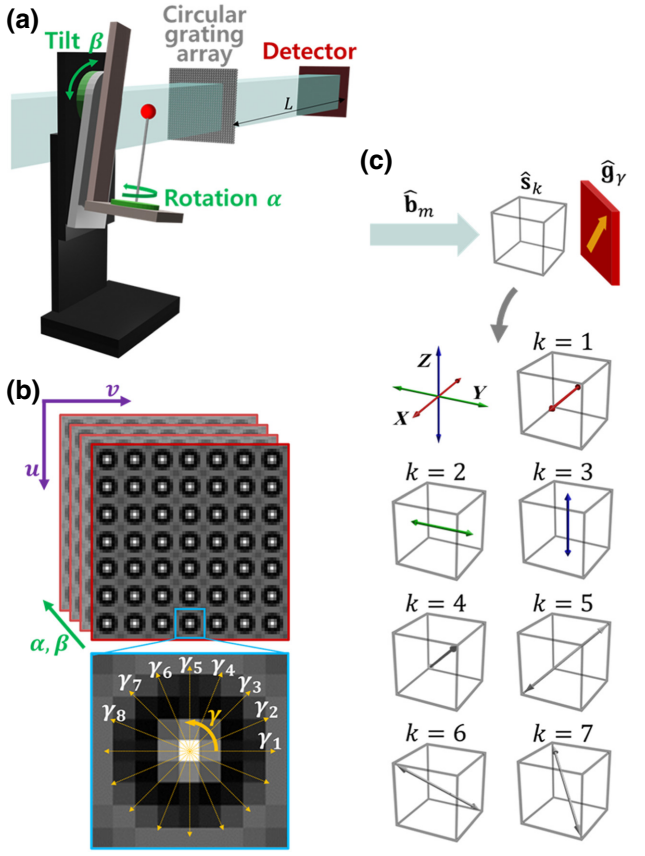

FIG. 1. (a) The x-ray scattering tensor tomography experimental setup. Images are acquired with the sample at the rotation angles α and tilt angles β. (b) The x rays are locally diffracted by the circular grating array and form a circular pattern at the detector. Each square box containing a single circular fringe is called a unit cell and each unit cell has an index (u, v). A unit cell consists of multiple detector pixels (a 9×9 detector grid in the schematic). The directional scattering signal is extracted along the sensitivity vectors $\hat{\mathbf{g}}_\gamma$ with an angle index γ. (c) The seven scattering sampling direction channels $\hat{\mathbf{s}}_k$ used in this study. The beam-direction vector is denoted as $\hat{\mathbf{b}}_m$.

II. METHODS

A. Derivation of algebraic filter for tensor tomography

A standard transmission (scalar) tomography or laminography problem with an arbitrary beam geometry can be generally expressed with a set of line integrals:

$$p_m = \int_{L_m} \mu(x) d\mathbf{x}, \tag{1}$$

where $\mu(x)$ is the attenuation coefficient as a function of $\mathbf{x} \in \mathbb{R}^3$ and L_m indicates the beam direction. The subscript m indicates the measurement for a rotation angle α, tilt angle β, and unit cell (u, v) [Figs. 1(a) and 1(b)]. Equation 1 is known as an x-ray transform and implies the Beer-Lambert law. It has been shown that the scattering signal can also be described based on the Beer-Lambert law [38–40], although the presence of multiple scattering could potentially result in additional noise if not treated rigorously [41]. Tensor-tomography problems involve additional dimensions due to the rotational dependence of the scattering signal [34]. The measured scattering signal depends not only on the sample orientation but also on the sensitivity direction angle, along which the directional scattering signals are extracted. Thus, a measured scattering signal $p_{m\gamma}$ with measurement index m and sensitivity angle index γ is expressed as

$$p_{m\gamma} = \sum_k v_{m\gamma k} \int_{L_m} \mu_k(x) d\mathbf{x}, \tag{2}$$

where the scalar term

$$v_{m\gamma k} \equiv (|\hat{\mathbf{b}}_m \times \hat{\mathbf{s}}_k| (\hat{\mathbf{s}}_k \cdot \hat{\mathbf{g}}_\gamma))^2 \tag{3}$$

takes the rotational dependence of the scattering signal into account [14]. The unit vector $\widehat{\mathbf{b}}_m$ represents the beam direction in the frame of the sample, which depends only on α and β for parallel-beam geometry. The unit vector $\widehat{\mathbf{g}}_\gamma$ represents the scattering-sensitivity direction, which depends on γ [Fig. 1(b)]. The unit vector $\widehat{\mathbf{s}}_k$ represents the scattering sampling direction along which the 3D scattering distribution is sampled [Fig. 1(c)]. We need to reconstruct the unknown $\mu_k(x) = |\mathbf{s}_k(\mathbf{x})|^2$, the squared magnitude of the scattering vector $\mathbf{s}_k$ along sampling channel k [14,34].

The measurements $p_{m\gamma}$ are collected for $M_\alpha \times M_\beta$ rotation and tilt angles and $M_u \times M_v$ unit cells [Figs. 1(a) and 1(b)], forming the measurement vector $\mathbf{p}_\gamma$, with $M = M_\alpha \times M_\beta \times M_u \times M_v$ elements. From Eq. (2), we form the forward-projection model in the discrete domain that describes the relation between $\mathbf{p}_\gamma \in \mathbb{R}^M$ and the reconstruction-volume vector $\boldsymbol{\mu}_k \in \mathbb{R}^N$, with N being the number of voxels of $\boldsymbol{\mu}_k$:

$$\begin{bmatrix} \mathbf{p}_1 \\ \vdots \\ \mathbf{p}_\gamma \\ \vdots \\ \mathbf{p}_\Gamma \end{bmatrix} = \begin{bmatrix} \mathbf{V}_{11}\mathbf{W} & \cdots & \mathbf{V}_{1K}\mathbf{W} \\ & \ddots & \\ \vdots & \mathbf{V}_{\gamma k}\mathbf{W} & \vdots \\ & \ddots & \\ \mathbf{V}_{\Gamma 1}\mathbf{W} & \cdots & \mathbf{V}_{\Gamma K}\mathbf{W} \end{bmatrix} \begin{bmatrix} \boldsymbol{\mu}_1 \\ \vdots \\ \boldsymbol{\mu}_k \\ \vdots \\ \boldsymbol{\mu}_K \end{bmatrix}, \tag{4}$$

where $\mathbf{V}_{\gamma k}$ is a diagonal $M \times M$ matrix with diagonal elements $v_{1\gamma k}, \ldots, v_{M\gamma k}$ [Eq. (3) and $\mathbf{W}$ is a sparse $M \times N$ matrix that represents the discrete beam-path-integral operation, so that it satisfies $\mathbf{p}_\gamma = \sum_k \mathbf{V}_{\gamma k}\mathbf{W}\mu_k$. Then, Eq. (4) can be rewritten as

$$\mathbf{p} = \left[\mathbf{V}_1\overline{\mathbf{W}} \cdots \mathbf{V}_k\overline{\mathbf{W}} \cdots \mathbf{V}_K\overline{\mathbf{W}}\right] \begin{bmatrix} \boldsymbol{\mu}_1 \\ \vdots \\ \boldsymbol{\mu}_k \\ \vdots \\ \boldsymbol{\mu}_K \end{bmatrix} = \mathbf{A}\mu, \tag{5}$$

where

$$\mathbf{V}_k\overline{\mathbf{W}} = \begin{bmatrix} \mathbf{V}_{1k} & \cdots & \mathbf{0} \\ \vdots & \ddots & \vdots \\ \mathbf{0} & \cdots & \mathbf{V}_{\Gamma k} \end{bmatrix} \begin{bmatrix} \mathbf{W} \\ \vdots \\ \mathbf{W} \end{bmatrix}. \tag{6}$$

The total measurement vector $\mathbf{p} = [\cdots; \mathbf{p}_\gamma; \cdots]$ for $\gamma = 1, 2, \ldots, \Gamma$, where the integer Γ is the total number of sensitivity angles, has $M' = M \times \Gamma$ elements. The vectorized reconstruction volume $\boldsymbol{\mu} = [\cdots; \boldsymbol{\mu}_k; \cdots]$ for $k = 1, 2, \ldots, K$, where K is the total number of sampling directions, has $N' = N \times K$ elements. Therefore, the size of the matrix $\mathbf{A}$ is $M' \times N'$.

Due to the rotational dependence of the scattering signal, so far only iterative reconstruction algorithms could be used to solve Eq. (5)—as, for example, in the simultaneous iterative reconstruction technique (SIRT) [34,42], for which the update equation at the η^{th} iteration is

$$\boldsymbol{\mu}^{(\eta+1)} = (\mathbf{I}_{N'} - \mathbf{C}\mathbf{A}^T\mathbf{R}\mathbf{A})\boldsymbol{\mu}^{(\eta)} + \mathbf{C}\mathbf{A}^T\mathbf{R}\mathbf{p}, \tag{7}$$

where $\mathbf{C}$ and $\mathbf{R}$ are $N' \times N'$ and $M' \times M'$ diagonal matrices with elements $c_{jj} = 1/\sum_i a_{ij}$ and $r_{ii} = 1/\sum_j a_{ij}$, respectively. The parameter a_{ij} is the element of $\mathbf{A}$ at the i^{th} row and j^{th} column. With $\boldsymbol{\mu}^{(0)} = \mathbf{0}$ as initial guess, the reconstructed volume vector can be expressed as follows [36,37]:

$$\boldsymbol{\mu} = \begin{bmatrix} \mathbf{I}_{N'} & \mathbf{0} \end{bmatrix} \begin{bmatrix} \mathbf{I}_{N'} - \mathbf{C}\mathbf{A}^T\mathbf{R}\mathbf{A} & \mathbf{C}\mathbf{A}^T\mathbf{R} \\ \mathbf{0} & \mathbf{I}_{M'} \end{bmatrix}^\eta \begin{bmatrix} \mathbf{0} \\ \mathbf{I}_{M'} \end{bmatrix} \mathbf{p}, \tag{8}$$

where $I_{N'}$ and $I_{M'}$ are identity matrices with dimensions $N' \times N'$ and $M' \times M'$. Equation (8) can be rewritten as $\boldsymbol{\mu} = \mathbf{Q}\mathbf{p}$, where $\mathbf{Q} = [\cdots; \mathbf{Q}_k; \cdots]$ is the reconstruction matrix for the SIRT–x-ray tensor tomography (XTT) algorithm at the η^{th} iteration step.

This iterative reconstruction can be approximated by a FBP with a precomputed algebraic filter. Let c be the index for the central voxel $\boldsymbol{\mu}_{c,k}$ of the reconstruction volume $\boldsymbol{\mu}_k$. Then, $\boldsymbol{\mu}_{c,k} = \mathbf{q}_k \cdot \mathbf{p}$, where $\mathbf{q}_k \in \mathbb{R}^{M'}$ is a row vector the elements of which correspond to the central row of $\mathbf{Q}_k$. For LSI reconstruction algorithms, both the reconstruction and the projection space can be shifted such that their relative positions with respect to an arbitrary voxel are the same as their relative original positions with respect to voxel c. It follows that the entire volume can be expressed as the back projection of the convolution of $\mathbf{q}_k$ with $\mathbf{p}$ and $\mathbf{q}_k$ is called the algebraic filter [36]. The volume vector $\boldsymbol{\mu}_k$ can then be reconstructed with FBP as

$$\boldsymbol{\mu}_k = \overline{\mathbf{W}}^T\mathbf{H}_{\mathbf{q}_k}\mathbf{p}, \tag{9}$$

where $\mathbf{H}_{\mathbf{q}_k}$ is the convolution matrix of the algebraic filter $\mathbf{q}_k$, with a size of $M' \times M'$. We dub this reconstruction method SIRT FBP XTT. An algebraic filter for tensor tomography is independent of the scanned sample and can approximate any linear-shift-invariant algebraic reconstruction algorithm.

B. Fast computation of the algebraic filter

Let us assume that we have $M_\alpha \times M_\beta = 500$ angular poses, $M_u \times M_v = 10^4$ detector pixels, $\Gamma = 10$ sensitivity directions, and $N = 1 \times 10^7$ voxels with $K = 7$ channels. Then, the size of $\mathbf{Q} \in \mathbb{R}^{N' \times M'}$ corresponds approximately to 14 petabyte, which is unpractical to store in memory; therefore, it is computed on the fly. The filter can be efficiently computed by multiplying an impulse $\boldsymbol{\delta} = [0, \ldots, 1, \ldots, 0] \in \mathbb{R}^n$ with the reconstruction matrix $\mathbf{Q}_k$,

so that

$$\mathbf{q}_k = \boldsymbol{\delta}_n \mathbf{Q}_k. \tag{10}$$

Thus, the total time required for computing a set of filters for SIRT FBP XTT is in the range of $\mathcal{O}(\tau \times K)$, i.e., K times the computation time for a single run of the algebraic reconstruction algorithm.

III. EXPERIMENTAL RESULTS

The proposed reconstruction method is validated with experiments performed at the TOMCAT beam line [43] of the Swiss Light Source, Switzerland. We acquire a data set for a fiber pellet assembly composed of industrially relevant fiber-reinforced materials. Each pellet has fibrous structures aligned along its axial direction and the micro-computed tomography (CT) validation data are shown in the Supplementary Information of Ref. [35]. The π-phase-shift circular grating array of the diffractive optics has a coarse period of $P = 49.5\ \mu$m with a fine-grating period of $g = 1.46\ \mu$m [32,34]. These phase optics do not effectively attenuate the beam: the zeroth and first-order components of the diffracted beam contribute mainly to the formation of circular fringes, with a peak intensity in the center of each unit cell. These optics work with a full-field beam and enable the acquisition of local 2D USAXS signals with omnidirectional sensitivity in a single shot. The sample is measured with a parallel monochromatic x-ray beam with 17 keV but the diffractive optics used do not have stringent requirements in terms of monochromaticity [32]. The projection data are taken with an FOV of 12.7 mm $\times$ 14.3 mm corresponding to 227 $\times$ 265 unit cells of 99 μm $\times$ 99 μm each. The exposure time for a projection image at each angular pose is 10 ms. The probed autocorrelation length ξ is 730 nm. The scattering angles 2θ in the range of $P/L = 50\ \mu$rad are probed with our setup, where $L = Pg/(2\lambda) \approx 49$ cm is the sample-to-detector distance and λ is the wavelength. No x-ray polarization is necessary for this experiment.

In the raw projection data, the circular fringe pattern in each unit cell is resolved with 9 $\times$ 9 detector pixel windows. The directional scattering signal, measured as the visibility reduction $D_{m\gamma}$ of the circular fringe with the measurement index m along the sensitivity angle with the index γ, is extracted as

$$D_{m\gamma} = \frac{V_{m\gamma,s}}{V_{m\gamma,f}} = \frac{\tilde{I}_{m\gamma,s}(2)/\tilde{I}_{m\gamma,s}(0)}{\tilde{I}_{m\gamma,f}(2)/\tilde{I}_{m\gamma,f}(0)}. \tag{11}$$

The visibility of the circular fringe $V_{m\gamma}$ is extracted with the angle index γ, where the subscripts f and s represent the flat measurement (without the sample) and the sample measurement, respectively, and $\tilde{I}_{m\gamma}(n)$ is the n^{th} component of the discrete Fourier transform of a unit-cell fringe in polar coordinates [32,34]. Then, our measurement scalar $p_{m\gamma} \in \mathbf{p} \in \mathbb{R}^{M'}$ is:

$$p_{m\gamma} = -\ln D_{m\gamma}. \tag{12}$$

A measured projection image is shown in Fig. 2(a).

We perform SIRT FBP XTT for the measured data according to Eq. (9). The considered angular geometric conditions are $\alpha \in \{0^\circ, 3.6^\circ, \ldots, 356.4^\circ\}$, $\beta \in \{0^\circ, 11.25^\circ, \ldots, 45^\circ\}$, and $\gamma \in \{-90^\circ, -67.5^\circ, \ldots, 67.5^\circ\}$. Three of the seven chosen scattering sampling directions $\widehat{\mathbf{s}}_k$ are parallel to the x, y, and z axes and the others to the four diagonals [Fig. 1(c)]. The reasons for choosing such a sampling scheme can be consulted in our previous study [35]. Different sets of filters are computed to approximate SIRT XTT with 5, 10, 25, 50, and 100 iterations. For comparison, we also perform SIRT XTT according to Eq. (8)

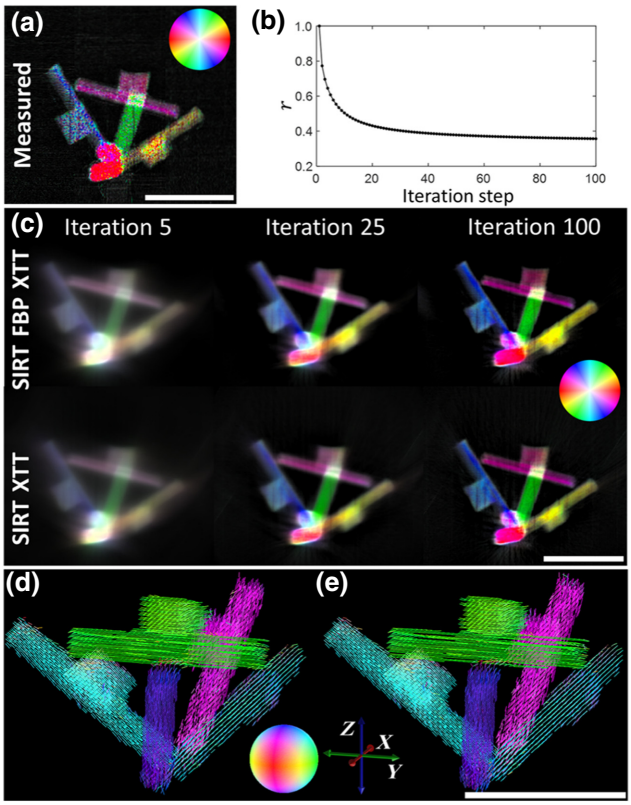

FIG. 2. (a) The measured projection image at an angular pose. For the color wheel, the HSV color scheme is used, where H (color) is the fiber orientation projected onto the detector plane, S (saturation) is the scattering anisotropy, and V (brightness) is the mean scattering intensity. (b) The residual norm curve. (c) A comparison of the forward projections of the SIRT-FBP-XTT and SIRT-XTT reconstructions. (d),(e) The three-dimensional (3D) rendering for the reconstructed fiber orientation using (d) SIRT FBP XTT and (e) SIRT XTT. The 3D color sphere maps the fiber orientation. The absolute values of the fiber orientation vector components $[x, y, z]$ correspond to the RGB values. Scale bar: 1 cm.

for the same data. The reconstructed volume size for both cases is $265 \times 265 \times 227$ with a voxel size of 99 μm.

The projection operations are performed utilizing the ASTRA Toolbox [44–46]. The reconstruction is run until convergence of r, the L_2 norm of the residual [Fig. 2(b)] $r = \|\mathbf{p} - \mathbf{A}\boldsymbol{\mu}\|_2^2$. The convergence is defined as less than 1% change of r between subsequent iterations. To evaluate the convergence better, we perform qualitative analysis of the reconstructed volumes. The results obtained with SIRT FBP XTT and SIRT XTT are compared in the projection space [Fig. 2(c)]: the forward-projection images of the two reconstructions look similar regardless of the iteration steps. After 50 iteration steps, both images look comparable to the measured projection image in Fig. 2(a). The 3D volume rendering of the reconstructed fiber orientation obtained with the two reconstruction methods are shown in Figs. 2(d) and 2(e). The two reconstructions obtained with SIRT FBP XTT and SIRT XTT show good qualitative agreement. The results indicate that SIRT FBP XTT with the computed algebraic filter accurately approximates the SIRT-XTT reconstruction.

For a quantitative comparison, we calculate the angular difference as $\Delta(\eta) = \arccos(\mathbf{o}_1(\eta) \cdot \mathbf{o}_2(\eta))$, where $\mathbf{o}_1(\eta)$ and $\mathbf{o}_2(\eta)$ are the normalized local fiber-orientation vectors reconstructed with SIRT FBP XTT and SIRT XTT. The angular difference $\Delta(\eta)$ is calculated for all voxels that correspond to the sample and the results are plotted in Fig. 3(a). Both the mean and median of $\Delta(\eta)$ are smaller than 2°, indicating that SIRT FBP XTT accurately approximates the established SIRT XTT.

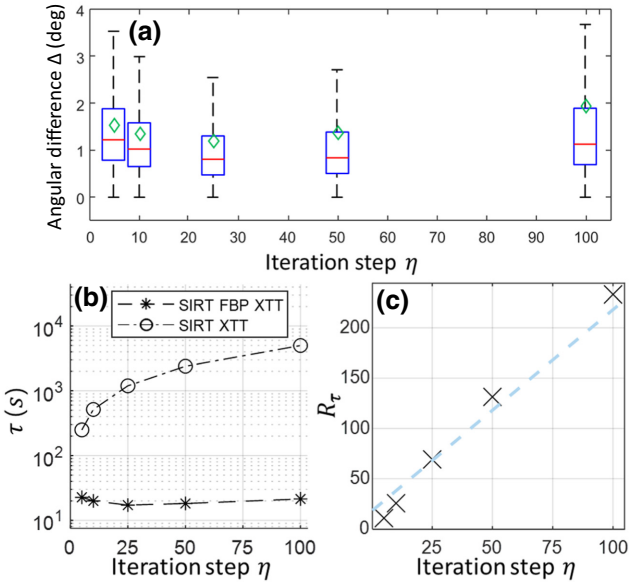

FIG. 3. (a) The distribution of the angular difference Δ between the reconstructed fiber orientation obtained with SIRT FBP XTT and SIRT XTT. The red lines and the green diamonds indicate the mean and median values of Δ, respectively. (b) The reconstruction time (τ) required by SIRT XTT and SIRT FBP XTT. (c) The ratio R_τ between the two reconstruction times. The dashed light blue line represents a linear fit to the data with a constant slope of 2.

To better compare the tensor-tomographic reconstruction time required for SIRT FBP XTT (τ_1) and SIRT XTT (τ_2) [Fig. 3(b)], their ratio R_τ as a function of the iteration step η is calculated as $R_\tau(\eta) = \tau_2(\eta)/\tau_1(\eta)$. This ratio increases almost linearly with η [Fig. 3(c)]. This observation matches exactly what is expected: SIRT FBP XTT requires only one back projection plus a convolution operation, while SIRT XTT requires η forward projections and η back projections. For $\eta = 100$, SIRT FBP XTT is more than 200 times faster than SIRT XTT. Considering that at least several tens of iteration steps are typically required for an algebraic reconstruction method, the reconstruction speed of the proposed method is at least a few orders of magnitude faster than the established methods, given the same computational resources. Assuming that 100 iterations are required, which take 1 h, for data with 100 time points, the computation time is reduced from 4.2 d to 30 min by using the proposed method. The fluctuations of τ for SIRT FBP XTT observed in Fig. 3(b) are due to the use of a shared computational cluster.

IV. CONCLUSIONS

We develop a direct filtered back-projection method based on algebraic filters that enables tensor-tomographic reconstructions that are significantly faster than when using conventional methods. The proposed method is compatible with arbitrarily complex acquisition trajectories. Any LSI algebraic algorithm, such as the simultaneous algebraic reconstruction technique (SART) [47], can also be chosen for the computation of the algebraic filters. Moreover, the proposed method is not only valid for the demonstrated experimental and reconstruction technique but also for any other tensor-tomographic imaging method (e.g., neutron imaging) that utilizes LSI algorithms. Numerous sets of filters for different acquisition geometries and problem sizes can be precomputed and stored in a long-term memory device. Appropriate filters can be loaded and applied to the projection data in an on-the-fly manner to provide a quick FBP reconstruction for tensor tomography.

So far, x-ray scattering tensor tomography has mostly been used, because of the inherently long acquisition and reconstruction time, only for proof-of-concept experiments on a few selected samples. The orders-of-magnitude reduction in computation time achieved by the proposed method, coupled with the recent experimental advancements [31–35], hopefully has the capacity to unleash the full potential of x-ray scattering tensor tomography and make this emerging technique invaluable for the investigation of multiple and larger samples as well as dynamic

(e.g., rheological) processes with hundreds of time points. The proposed method enables rapid feedback and control for tensor-tomography experiments, hopefully opening up new perspectives for the deep understanding of the fundamental link between functional material properties and microarchitecture.

ACKNOWLEDGMENTS

We would like to thank Poulami Somanya Ganguly, Centrum Wiskunde & Informatica and Leiden University, for her contribution and valuable discussions for initiating this project. This work received funding from the European Union Horizon 2020 Marie Skłodowska-Curie Grant No. 765604 ["MUltiscale, Multimodal and Multidimensional imaging for EngineeRING" (MUMMERING)]. D.M.P. is supported by The Netherlands Organisation for Scientific Research (NWO), project number 016.Veni.192.235. We acknowledge the Paul Scherrer Institut, Villigen, Switzerland for the provision of synchrotron radiation beam time at the TOMCAT beam line of the Swiss Light Source. We thank Xnovo Technology ApS, Denmark for providing the fiber-pellet assembly.

[1] P. Fratzl, in *Collagen: Structure and Mechanics*, edited by P. Fratzl (Springer US, Boston, Massachusetts, 2008), p. 1.

[2] M. A. Meyers, J. McKittrick, and P. Y. Chen, Structural biological materials: Critical mechanics-materials connections, Science **339**, 773 (2013).

[3] J. J. Martin, B. E. Fiore, and R. M. Erb, Designing bioinspired composite reinforcement architectures via 3D magnetic printing, Nat. Commun. **6**, 8641 (2015).

[4] J. Song, *et al.*, Processing bulk natural wood into a high-performance structural material, Nature **554**, 224 (2018).

[5] S. Jbabdi, S. N. Sotiropoulos, S. N. Haber, D. C. Van Essen, and T. E. Behrens, Measuring macroscopic brain connections *in vivo*, Nat. Neurosci. **18**, 1546 (2015).

[6] R. Byron Pipes, R. L. McCullough, and D. G. Taggart, Behavior of discontinuous fiber composites: Fiber orientation, Polym. Compos. **3**, 34 (1982).

[7] S. Abbasi, P. J. Carreau, and A. Derdouri, Flow induced orientation of multiwalled carbon nanotubes in polycarbonate nanocomposites: Rheology, conductivity and mechanical properties, Polymer **51**, 922 (2010).

[8] R. M. Auenhammer, L. P. Mikkelsen, L. E. Asp, and B. J. Blinzler, Automated x-rayMUltiscale, Multimodal and Multidimensional imaging for EngineeRING computer tomography segmentation method for finite element analysis of non-crimp fabric reinforced composites, Compos. Struct. **256**, 113136 (2021).

[9] C. E. Shannon, Communication in the presence of noise, Proc. IRE **37**, 10 (1949).

[10] W. Yashiro, Y. Terui, K. Kawabata, and A. Momose, On the origin of visibility contrast in x-ray Talbot interferometry, Opt. Express **18**, 16890 (2010).

[11] S. K. Lynch, V. Pai, J. Auxier, A. F. Stein, E. E. Bennett, C. K. Kemble, X. Xiao, W. Keat Lee, N. Y. Morgan, and H. H. Wen, Interpretation of dark-field contrast and particle-size selectivity in grating interferometers, Appl. Opt. **50**, 4310 (2011).

[12] M. Strobl, General solution for quantitative dark-field contrast imaging with grating interferometers, Sci. Rep. **4**, 7243 (2014).

[13] N. Stribeck, A. A. Camarillo, U. Nöchel, C. Schroer, M. Kuhlmann, S. V. Roth, R. Gehrke, and R. K. Bayer, Volume-resolved nanostructure survey of a polymer part by means of SAXS microtomography, Macromol. Chem. Phys. **207**, 1139 (2006).

[14] A. Malecki, G. Potdevin, T. Biernath, E. Eggl, K. Willer, T. Lasser, J. Maisenbacher, J. Gibmeier, A. Wanner, and F. Pfeiffer, X-ray tensor tomography, EPL **105**, 38002 (2014).

[15] F. L. Bayer, S. Hu, A. Maier, T. Weber, G. Anton, T. Michel, and C. P. Riess, Reconstruction of scalar and vectorial components in x-ray dark-field tomography, Proc. Natl. Acad. Sci. USA **111**, 12699 (2014).

[16] M. Liebi, M. Georgiadis, A. Menzel, P. Schneider, J. Kohlbrecher, O. Bunk, and M. Guizar-Sicairos, Nanostructure surveys of macroscopic specimens by small-angle scattering tensor tomography, Nature **527**, 349 (2015).

[17] F. Schaff, M. Bech, P. Zaslansky, C. Jud, M. Liebi, M. Guizar-Sicairos, and F. Pfeiffer, Six-dimensional real and reciprocal space small-angle x-ray scattering tomography, Nature **527**, 353 (2015).

[18] M. Wieczorek, F. Schaff, F. Pfeiffer, and T. Lasser, Anisotropic X-Ray Dark-Field Tomography: A Continuous Model and its Discretization, Phys. Rev. Lett. **117**, 158101 (2016).

[19] E. T. Skjønsfjell, T. Kringeland, H. Granlund, K. Høydalsvik, A. Diaz, and D. W. Breiby, Retrieving the spatially resolved preferred orientation of embedded anisotropic particles by small-angle x-ray scattering tomography, J. Appl. Crystallogr. **49**, 902 (2016).

[20] M. Georgiadis, M. Guizar-Sicairos, O. Gschwend, P. Hangartner, O. Bunk, R. Müller, and P. Schneider, Ultrastructure organization of human trabeculae assessed by 3D sSAXS and relation to bone microarchitecture, PLoS ONE **11**, e0159838 (2016).

[21] C. Jud, F. Schaff, I. Zanette, J. Wolf, A. Fehringer, and F. Pfeiffer, Dentinal tubules revealed with x-ray tensor tomography, Dent. Mater. **32**, 1189 (2016).

[22] M. Georgiadis, *et al.*, Nanostructure-specific x-ray tomography reveals myelin levels, integrity and axon orientations in mouse and human nervous tissue, Nat. Commun. **12**, 2941 (2021).

[23] Y. Sharma, F. Schaff, M. Wieczorek, F. Pfeiffer, and T. Lasser, Design of acquisition schemes and setup geometry for anisotropic x-ray dark-field tomography (AXDT), Sci. Rep. **7**, 3195 (2017).

[24] J. Kim, A. Slyamov, E. Lauridsen, M. Birkbak, T. Ramos, F. Marone, J. W. Andreasen, M. Stampanoni, and M. Kagias, Macroscopic mapping of microscale fibers in freeform injection molded fiber-reinforced composites using x-ray scattering tensor tomography, Compos. Part B: Eng. **233**, 109634 (2022).

[25] J. M. Feldkamp, M. Kuhlmann, S. V. Roth, A. Timmann, R. Gehrke, I. Shakhverdova, P. Paufler, S. K. Filatov,

R. S. Bubnova, and C. G. Schroer, Recent developments in tomographic small-angle x-ray scattering, Phys. Status Solidi (A) Appl. Mater. Sci. **206**, 1723 (2009).

[26] F. Schaff, F. Prade, Y. Sharma, M. Bech, and F. Pfeiffer, Non-iterative directional dark-field tomography, Sci. Rep. **7**, 3307 (2017).

[27] J. Vogel, F. Schaff, A. Fehringer, C. Jud, M. Wieczorek, F. Pfeiffer, and T. Lasser, Constrained x-ray tensor tomography reconstruction, Opt. Express **23**, 15134 (2015).

[28] M. Liebi, M. Georgiadis, J. Kohlbrecher, M. Holler, J. Raabe, I. Usov, A. Menzel, P. Schneider, O. Bunk, and M. Guizar-Sicairos, Small-angle x-ray scattering tensor tomography: Model of the three-dimensional reciprocal-space map, reconstruction algorithm and angular sampling requirements, Acta Crystallogr., Sect. A: Found. Adv. **74**, 12 (2018).

[29] S. Seyyedi, M. Wieczorek, F. Pfeiffer, and T. Lasser, Incorporating a noise reduction technique into x-ray tensor tomography, IEEE Trans. Comput. Imaging **4**, 137 (2018).

[30] Z. Gao, M. Guizar-Sicairos, V. Lutz-Bueno, A. Schröter, M. Liebi, M. Rudin, and M. Georgiadis, High-speed tensor tomography: Iterative reconstruction tensor tomography (IRTT) algorithm, Acta Crystallogr., Sect. A: Found. Adv. **75**, 223 (2019).

[31] M. Kagias, Z. Wang, P. Villanueva-Perez, K. Jefimovs, and M. Stampanoni, 2D-Omnidirectional Hard-X-Ray Scattering Sensitivity in a Single Shot, Phys. Rev. Lett. **116**, 093902 (2016).

[32] M. Kagias, Z. Wang, M. E. Birkbak, E. Lauridsen, M. Abis, G. Lovric, K. Jefimovs, and M. Stampanoni, Diffractive small angle x-ray scattering imaging for anisotropic structures, Nat. Commun. **10**, 5130 (2019).

[33] M. Kagias, Z. Wang, G. Lovric, K. Jefimovs, and M. Stampanoni, Simultaneous Reciprocal and Real Space X-Ray Imaging of Time-Evolving Systems, Phys. Rev. Appl. **15**, 044038 (2021).

[34] J. Kim, M. Kagias, F. Marone, and M. Stampanoni, X-ray scattering tensor tomography with circular gratings, Appl. Phys. Lett. **116**, 134102 (2020).

[35] J. Kim, M. Kagias, F. Marone, Z. Shi, and M. Stampanoni, Fast acquisition protocol for x-ray scattering tensor tomography, Sci. Rep. **11**, 23046 (2021).

[36] K. J. Batenburg and L. Plantagie, Fast approximation of algebraic reconstruction methods for tomography, IEEE Trans. Image. Process. **21**, 3648 (2012).

[37] D. M. Pelt and V. De Andrade, Improved tomographic reconstruction of large-scale real-world data by filter optimization, Adv. Struct. Chem. Imaging **2**, 17 (2016).

[38] M. Bech, O. Bunk, T. Donath, R. Feidenhans'l, C. David, and F. Pfeiffer, Quantitative x-ray dark-field computed tomography, Phys. Med. Biol. **55**, 5529 (2010).

[39] V. Revol, C. Kottler, R. Kaufmann, A. Neels, and A. Dommann, Orientation-selective x-ray dark field imaging of ordered systems, J. Appl. Phys. **112**, 114903 (2012).

[40] A. Malecki, G. Potdevin, T. Biernath, E. Eggl, E. G. Garcia, T. Baum, P. B. Noël, J. S. Bauer, and F. Pfeiffer, Coherent superposition in grating-based directional dark-field imaging, PLoS ONE **8**, e61268 (2013).

[41] P. Modregger, M. Kagias, S. Peter, M. Abis, V. A. Guzenko, C. David, and M. Stampanoni, Multiple Scattering Tomography, Phys. Rev. Lett. **113**, 020801 (2014).

[42] P. Gilbert, Iterative methods for the three-dimensional reconstruction of an object from projections, J. Theor. Biol. **36**, 105 (1972).

[43] M. Stampanoni, A. Groso, A. Isenegger, G. Mikuljan, Q. Chen, D. Meister, M. Lange, R. Betemps, S. Henein, and R. Abela, in *AIP Conference Proceedings*, Vol. 879 (AIP Publishing, Sine Loco, 2007), p. 848.

[44] W. van Aarle, W. J. Palenstijn, J. De Beenhouwer, T. Altantzis, S. Bals, K. J. Batenburg, and J. Sijbers, The ASTRA Toolbox: A platform for advanced algorithm development in electron tomography, Ultramicroscopy **157**, 35 (2015).

[45] W. van Aarle, W. Jan Palenstijn, J. Cant, E. Janssens, F. Bleichrodt, A. Dabravolski, J. De Beenhouwer, K. Joost Batenburg, and J. Sijbers, Fast and flexible x-ray tomography using the ASTRA Toolbox, Opt. Express **24**, 25129 (2016).

[46] W. J. Palenstijn, K. J. Batenburg, and J. Sijbers, Performance improvements for iterative electron tomography reconstruction using graphics processing units (GPUs), J. Struct. Biol. **176**, 250 (2011).

[47] A. H. Andersen and A. C. Kak, Simultaneous algebraic reconstruction technique (SART): A superior implementation of the art algorithm, Ultrason. Imaging **6**, 81 (1984).